Appl. Phys. B 86, 633–642 (2007)
DOI: 10.1007/s00340-006-2546-x

Applied Physics B
Lasers and Optics

J.-M. MELKONIAN[1,✉]
A. GODARD[1]
M. LEFEBVRE[1]
E. ROSENCHER[1,2]

Pulsed optical parametric oscillators with intracavity optical parametric amplification: a critical study

[1] Office National d'Études et de Recherches Aéropatiales, Chemin de la Hunière, 91761 Palaiseau Cedex, France
[2] Département de Physique, École Polytechnique, 91128 Palaiseau Cedex, France

Received: 10 July 2006/Final version: 13 November 2006
Published online: 23 December 2006 • © Springer-Verlag 2006

ABSTRACT It is known that the idler conversion efficiency of optical parametric oscillators (OPOs) can be increased by adding a second nonlinear crystal in the cavity. This crystal is pumped by the signal and acts as an optical parametric amplifier (OPA) for the idler. However, this technique unavoidably increases the oscillation threshold because of additional losses and increased build-up time due to cavity lengthening. In this paper, we investigate both theoretically and experimentally the benefits and drawbacks of this so called OPO–OPA configuration versus the singly resonant OPO (SRO) configuration. Calculations are found to be in agreement with an experimental study of a SRO and an OPO–OPA operating near 3.4 μm both pumped by a 90-mJ 27-ns Nd:YAG laser. Our study reveals that the OPO–OPA needs to be driven at least two times above threshold to produce more idler energy than the SRO. In addition, near 3 μm the OPO–OPA is particularly efficient given that the difference frequency wave generated in the second crystal is also output coupled.

PACS 42.65.Yj; 42.65.Sf

1 Introduction

Optical parametric oscillators (OPOs) are efficient devices to generate coherent light at wavelengths where lasers perform poorly or are unavailable. OPOs downconvert a pump light of frequency ω_p into two tunable frequencies, signal frequency ω_s and idler frequency ω_i, through a nonlinear three-wave mixing process such as $\omega_p = \omega_s + \omega_i$ with $\omega_i < \omega_s$ (cf. Fig. 1a). OPOs are of particular interest for the production of mid-infrared radiation where molecular species have their fundamental absorption features [1]. The production of medium energy pulses (several millijoules) in the mid-IR (around 3 μm) is also of high interest to detect defects in composite materials. Indeed, it was demonstrated that mid-IR radiation is well-suited to efficiently generate ultrasonic waves for the inspection of polymer-matrix composites [2–5].

In most cases, only the idler wavelength stands within the mid-IR domain, while the signal radiation is useless, which limits the maximum optical-to-optical conversion efficiency to the pump to idler frequency ratio $\omega_i/\omega_p < 50\%$. Hence, for the conversion of 1-μm laser emission to a 3-μm wavelength, the efficiency is limited to 30%. Moreover, under pulsed operation, the practical pump to idler energy conversion efficiency reduces to values of about 10%–15% due to the finite build-up time of the parametric oscillation.

An attractive approach to overcome this limitation is to combine the parametric interaction with intracavity difference-frequency mixing (DFM) [6–8] such that the difference frequency ω_d is given by $\omega_d = \omega_s - \omega_i$ (cf. Fig. 1b). Basically, DFM acts as an optical parametric amplification (OPA) process for the idler radiation with the signal as a pump wave [9]. Using this configuration, referred as OPO–OPA, it is thus possible to increase the idler conversion efficiency. Moreover, the difference frequency radiation produced by the OPO–OPA can be made close or equal to the idler, thus increasing the total mid-IR energy.

The OPO–OPA configuration was first proposed by Koch et al. in a theoretical paper [6]. Using a plane-wave continuous-wave (cw) model, the authors predicted an idler photon-conversion efficiency higher than 100% over a large dynamic range of incident pump intensity, for a proper choice of the ratio of the nonlinear coupling parameters between the OPO and OPA processes. Later, the same group experimentally demonstrated an idler photon-conversion efficiency of 110% implementing the technique in the picosecond regime [7]. Next, improvement of the idler quantum efficiency was demonstrated in the nanosecond regime with a Nd:YAG-pumped OPO–OPA based on two PPLN crystals [8]. The authors obtained as much as 57 μJ at 3.8 μm for 211 μJ pump energy, i.e., 96% pump photon conversion efficiency. Higher idler energy of 310 μJ was then obtained at 3.4 μm (with a lower overall photon efficiency of 76%) in [9].

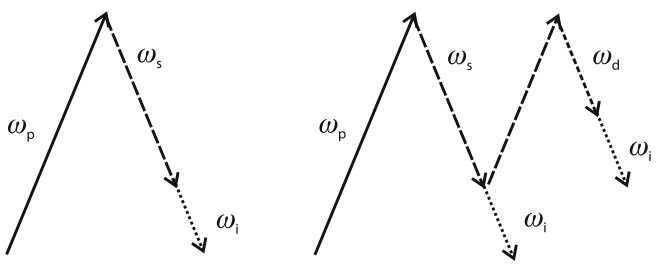

FIGURE 1 Frequency diagrams of (**a**) OPO and (**b**) OPO–OPA

✉ Fax: +33 1 6993 6182, E-mail: jean-michel.melkonian@onera.fr

However, these studies were led with highly nonlinear crystals of limited aperture, and thus at low pump energy. For mid-energy OPOs, it is required to use large aperture crystals. At the present time, it is still more convenient to use less efficient materials such as KTP or KTA that offer a higher damage threshold and a lower cost than large section PPLN crystal which cannot yet be considered as reliable commercial products. However, because the above-mentioned crystals exhibit limited nonlinear efficiencies, their insertion in the OPO cavity may significantly increase the oscillation threshold. Indeed, the OPA crystal introduces losses and enlarges the build-up time which results from the OPO cavity lengthening. This last feature is unavoidable and cannot be neglected in the nanosecond regime because of the limited number of available cavity round-trips.

A singly resonant OPO (SRO) with the same mirrors as the OPO–OPA but a shorter cavity including only the OPO crystal will thus exhibit a lower oscillation threshold. However, thanks to its higher optical gain the OPO–OPA will eventually overtake the SRO from a given amount of pump energy onwards. The purpose of this paper is to investigate both theoretically and experimentally the potentiality of the OPO–OPA configuration and its limitation versus the usual SRO configuration in the nanosecond transient regime. Two cases are considered; firstly, we focus on the generated idler energy at 3.45 μm; secondly, we consider pumping conditions such that both idler and difference-frequency radiations stands within the mid-IR domain, so that the total useful energy is located at 3.45 μm and 2.78 μm. This second situation could be particularly useful for applications like laser ultrasound generation that have a broad spectral acceptance around 3 μm [5].

A theoretical study is first carried out in Sect. 2 using the general three-wave mixing approach that exactly takes into account the nonlinear interactions between the waves in the nonlinear crystals [10]. This study relies on the formalism developed in [11] for cw regime and in [12] for pulsed regime. It is extended to the OPO–OPA scheme and fully includes pump depletion, back-reconversion effects, as well as imperfect phase-matching in the OPA crystal. This formalism allows us to discuss the main qualitative features of the OPO–OPA scheme in the plane-wave approximation. The expressions obtained in the steady-state limit are in agreement with [6]. We also derive an analytical expression of the optimal ratio of the nonlinear couplings of the two crystals. Then we show how this optimal ratio leads to an increase of the OPO–OPA performance in the pulsed regime. Finally we include the spatial distribution of the pump beam in order to compare quantitatively simulation and experimental results.

In our experimental study of Sect. 3, we design several OPO configurations and report on the obtained performances. The first studied configuration is a single-crystal short-cavity SRO. This configuration is then modified step by step to eventually implement a two-crystal OPO–OPA device. In all cases a 27-ns 90-mJ Nd:YAG laser is used as the pump source and potassium titanyl arsenate (KTA) crystals are used as the nonlinear material.

Simulation and experimental results are finally discussed in Sect. 4 in order to determine the potentiality of the OPO–OPA in the context of mid-energy pulsed OPOs.

2 OPO–OPA theory and simulation

2.1 *Determination of the optimum* OPO–OPA *design*

In this subsection, we determine the optimal ratio of the nonlinear couplings of the two crystals. An analytical expression is derived in the steady-state regime under the plane-wave approximation, using the formalism proposed in [11].

We consider the configuration depicted in Fig. 2 with absorptionless crystals and perfect coatings. Input and output mirrors have a reflectivity R at the signal wavelength.

In order to establish simple and universal expressions, we first introduce the normalized variables $X = \varphi_\mathrm{p}/\varphi_\mathrm{th}^\mathrm{cw}$, $Y = \varphi_\mathrm{s}/\varphi_\mathrm{th}^\mathrm{cw}$, and $Z = \varphi_\mathrm{i}/\varphi_\mathrm{th}^\mathrm{cw}$ (see also Table 1), where $\varphi_\mathrm{p,s,i}$ are respectively the intracavity pump, signal, and idler photon flux, and where $\varphi_\mathrm{th}^\mathrm{cw}$ is the singly-resonant OPO threshold in cw regime given by [11]

$$\varphi_\mathrm{th}^\mathrm{cw} = \frac{1}{2\hbar Z_0}\left[\frac{\operatorname{arccosh}\left(1/\sqrt{R}\right)}{\kappa_1 L_1}\right]^2 . \tag{1}$$

In (1), $\hbar$ is the Planck constant, $Z_0 = \mu_0 c$ is the vacuum impedance (377 Ω), L_1 is the length of the first crystal, and κ_1 is the nonlinear coupling coefficient given by

$$\kappa_1 = \frac{d_\mathrm{eff}}{c}\left(\frac{\omega_\mathrm{i}\omega_\mathrm{s}\omega_\mathrm{p}}{n_\mathrm{i}n_\mathrm{s}n_\mathrm{p}}\right)^{1/2} , \tag{2}$$

where c is the speed of light in vacuum, d_eff is the nonlinear coefficient, and $n_\mathrm{i,s,p}$ are the refraction indices of the first crystal at the idler, signal, and pump wavelengths, respectively.

The exact solutions of the coupled nonlinear equations describing the propagation of the three waves in the crystals can be derived following the approach presented in [10]. In this way, one can find an analytical expression of the parametric gain $G_1(X_0, Y_0) = Y_1/Y_0$ experienced by signal Y from z_0 to z_1, assuming perfect phase matching in the first crystal. For legibility's sake, the expression (A.1) of $G_1(X_0, Y_0)$, which involves Jacobi sine functions, is reported in Appendix A.

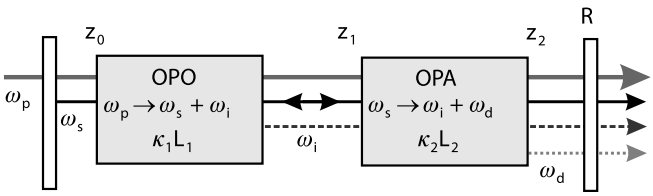

FIGURE 2 Schematic diagram of the OPO–OPA cavity with the notation used in this paper

Quantity	Symbol
Pump	X
Intracavity signal	Y
Idler	Z
Difference-frequency	D
Time	T

TABLE 1 Notation of normalized variables

With the same approach, one can also establish the expression of the parametric gain $G_2(Y_1, Z_1, \gamma, \Theta) = Z_2/Z_1$ experienced by the idler wave from z_1 to z_2. It involves new parameters $\gamma = \kappa_2 L_2/\kappa_1 L_1$ and Θ that are respectively the ratio of the nonlinear drives of the second crystal (OPA) to the first crystal (OPO) and the dimensionless phase-mismatch in the OPA crystal. The expressions (A.3) of $G_2(Y_1, Z_1, \gamma, \Theta) = Z_2/Z_1$ and (A.6) of Θ are given in Appendix A.

The nonlinear loss (depletion) of signal from z_1 to z_2 thus reads

$$Y_2 = Y_1 - Z_1 \left[G_2(Y_1, Z_1, \gamma, \Theta) - 1\right], \tag{3}$$

which yields the overall gain $G(X_0, Y_0, \gamma, \Theta) = Y_2/Y_0$ experienced by the signal wave through the two nonlinear crystals

$$G(X_0, Y_0, \gamma, \Theta) = G_1(X_0, Y_0) - [G_1(X_0, Y_0) - 1] \times (G_2\{G_1(X_0, Y_0)Y_0, [G_1(X_0, Y_0) - 1]Y_0, \gamma, \Theta\} - 1). \tag{4}$$

With the above expressions, one can carry out a general theoretical study with arbitrary mirrors reflectivities and pumping levels where the mean-field or constant-signal approximation is known to significantly deviate from exact solutions [11, 13–16]. Indeed, as shown in Sect. 3, the losses are not negligible in actual OPO–OPA devices.

The optimal ratio of the nonlinear couplings of the two crystals is determined in the steady-state regime in order to obtain an analytical expression. The oscillation condition is then given by the following implicit equation

$$G(X_0, Y_0, \gamma, \Theta) = 1/R. \tag{5}$$

Equation (5) gives the value of the normalized signal flux Y_0 at position $z = z_0$ as a function of the input pump flux X_0. One can then straightforwardly calculate depleted pump X_2, output signal Y_2, output idler Z_2, and output difference-frequency D_2 as functions of X_0 and Y_0 using the expressions given in Appendix B.

This equation is very useful since it allows us to find the proper ratio γ of the nonlinear couplings of the two crystals. Indeed, it was shown numerically in [6] that an optimum value $\gamma_{\rm cpd}$ of this ratio allowed for complete pump depletion (CPD) over a wide dynamical range and thus a maximum idler energy. In the case of perfect phase-matching in the OPA crystal ($\Delta k L_2/2 = 0$ or $\Theta = 0$), this value was close to $\gamma = 0.5$ for $R = 0.9$. For imperfect phase-matching, it was also shown that the value of $\gamma_{\rm cpd}$ slightly increased leading to $\gamma_{\rm cpd} \simeq 0.6$ for $\Delta k L_2/2 = 1$. With our formalism, an approached value of $\gamma_{\rm cpd}$ can be obtained for $R \to 1$, solving the following equation that directly involves simple parameters as Δk or X_0

$$\gamma_{\rm cpd} = \frac{2}{\pi}\left[1 - \left(\frac{\Delta k L_2}{\pi \gamma_{\rm cpd}}\right)^2\right]^{-1/2} \times \operatorname{arcsinh}\left\{\left(1 - \frac{\pi^2}{4X_0}\right)^{1/2}\left[1 - \left(\frac{\Delta k L_2}{\pi \gamma_{\rm cpd}}\right)^2\right]^{1/2}\right\}. \tag{6}$$

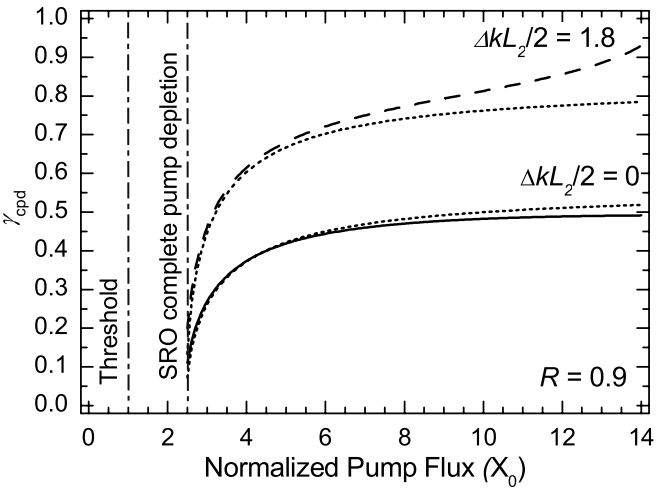

FIGURE 3 Values of parameters $\gamma = \kappa_2 L_2/\kappa_1 L_1$ that yield complete pump depletion as functions of normalized input pump flux. The *solid line* corresponds to a perfect phase matching in the second crystal while the *dashed curve* is for a phase mismatch of 1.8. *Dotted curves* are obtained by use of the approximated expression (6)

In the case of perfect phase-matching in the second crystal, this equation dramatically simplifies

$$\gamma_{\rm cpd} = \frac{2}{\pi}\operatorname{arcsinh}\left[\left(1 - \frac{\pi^2}{4X_0}\right)^{1/2}\right]. \tag{7}$$

The derivation of (6) requires some elliptic function algebra detailed in Appendix C. Besides, one should note that, since $R \to 1$ is assumed to establish (6), the same result can be obtained by use of the mean-field approximation, which is demonstrated in Appendix D. As shown in Fig. 3, the values of $\gamma_{\rm cpd}$ given by (6) are very close to the values of $\gamma_{\rm cpd}$ obtained by a full numerical solving when CPD is imposed in the OPO–OPA implicit equations when the pump power is not too high. The deviation becomes larger for higher pump power (when the mean-field approximation is becoming questionable) and for higher loss; however, it remains better than 10% for $R > 0.8$ and $X < 10$. Relation (6) is thus very useful even for practical design since the corresponding value of $\gamma_{\rm cpd}$ will lead to an improved conversion efficiency over a large dynamic range of transverse or temporal intensity variations. As a consequence, the optimal value of γ obtained with this expression is still valid in the pulsed regime, as we will see in the next subsection.

2.2 *Plane wave analysis of the pulsed regime*

In transient regime, the value of the intracavity signal at pass n, $Y_0^{(n)}$, and the value of the signal at the next pass, $Y_0^{(n+1)}$, are related by the following recurrent equation

$$Y_0^{(n+1)} = RG\left(X_0^{(n)}, Y_0^{(n)}, \Theta\right) Y_0^{(n)}. \tag{8}$$

Assuming that $\mathrm{d}Y/\mathrm{d}t \approx \left(Y^{(n+1)} - Y^{(n)}\right)/\tau$ where τ is the cavity round-trip time, (8) can be rewritten as the following differential time equation

$$\frac{\mathrm{d}Y}{\mathrm{d}T} + (1 - R)(Y - Y_{\rm noise}) = R\left[G(X, Y, \Theta) - 1\right] Y, \tag{9}$$

where $T\ (=t/\tau)$ is the normalized time unit and where subscript "0" has been omitted. Clearly, when the input pump power is switched off, the signal power decays to the noise level Y_{noise} with a characteristic time scale $\tau_{\text{cav}} = \tau/(1-R)$ that corresponds to the photons lifetime in the cavity. The term in the right-hand side of (9) is the nonlinear driving term related to the pumping of the OPO–OPA cavity.

The input pump temporal profile is assumed to be a Gaussian shape of maximum amplitude X_{peak} at the time T_0, with a full width at half maximum ΔT

$$X(T) = X_{\text{peak}}(\Delta T)\exp\left[\frac{-4\ln 2}{\Delta T^2}(T-T_0)^2\right]. \tag{10}$$

The temporal behavior of the resonant wave $Y(T)$ can thus be easily obtained by numerical integration of (9), with the initial condition $Y(0) = Y_{\text{noise}}$ assuming half a photon per mode. The corresponding output flux (signal, idler, difference-frequency, and depleted pump) can then be directly obtained using the expressions (B.1)–(B.4) given in Appendix B.

To compare SRO and OPO–OPA configurations in pulsed regime, we now consider that the OPO–OPA's cavity is longer than the SRO's, resulting in a shorter input pump pulse duration: $\Delta T = 40$ for OPO–OPA and $\Delta T_{\text{sro}} = 55$ for SRO. These selected values of the pulse duration are chosen to be close to the experimental conditions studied in Sect. 3. We also increase the cavity loss to $R = 0.8$, assuming perfect phase-matching in the OPA crystal and set $\gamma = 0.5$. Figure 4 presents the corresponding input–output characteristics where we plot the pulses averaged photon flux given by $\langle x\rangle = (1/\Delta T)\int x(T)\,\mathrm{d}T$.

As seen in Fig. 4, in the pulsed regime the threshold of the SRO is smaller than the one of the OPO–OPA because of its shorter cavity length. However, the SRO saturates strongly whereas there is no noticeable saturation for the OPO–OPA. In this way, the OPO–OPA eventually overtakes the SRO for pumping levels larger than 1.6 times threshold in the considered case. The physical reason for this is that the nonlinear gain experienced by the resonating signal wave in the OPO crystal is balanced by the nonlinear loss in the OPA crystal. This way, the normalized signal flux is kept close to the optimal value ($(1-R)Y_0 \simeq \pi^2/2$ in the steady-state regime, see Appendix C) that leads to CPD over a large dynamic range. In Fig. 5a, which depicts the temporal profiles of the different waves, we can see that this effect leads to an instantaneous photon conversion efficiency close to 200% in the OPO–OPA. Almost every pump photon is converted accordingly to the process depicted in Fig. 1b. Additionally, back-conversion is negligible because quasi-CPD can be achieved over a large dynamical range. This does not occur with the SRO, for which CPD occurs only transitorily, as shown in Fig. 5b. Furthermore, as shown in Fig. 4, where we also plot the total number of mid-IR photon flux $\langle Z_2\rangle + \langle D_2\rangle$, the potential superiority of the OPO–OPA is even more apparent in the context of applications such as laser ultrasound where all the mid-IR radiation is useful. To obtain these results, it is important to choose an appropriate value γ_{cpd} for the nonlinear couplings ratio. This value is determined by (7). As said before, it is still valid in the pulsed regime. We checked further this assertion by running the simulation of Fig. 4 with different values of γ and found no noticeable improvement ($> 5\%$) in the idler output power.

Let us now consider the case of a too long or too efficient OPA crystal. The nonlinear loss is now too strong for perfect phase-matching ($\Delta k L_2/2 = 0$): the efficiency decreases and CPD never occurs. It can be shown that efficient operation is recovered by use of a relevant phase-mismatch in the OPA crystal. The phase-mismatch value is chosen to satisfy (6) for large values of X_0 (see Fig. 3) in order to achieve quasi-complete pump depletion over a wide range. For instance, an OPO–OPA with $\gamma = 0.8$ and a phase-mismatch of $\Delta k L_2/2 = 1.8$ yields input–output curves which are not discernible from those obtained in Fig. 4.

On the other hand, CPD cannot be achieved for large values of X_0 if parameter γ is too small (typically if $\gamma < 0.5$). Hence in practice it is preferable to implement an OPA crystal that is too long rather than too short.

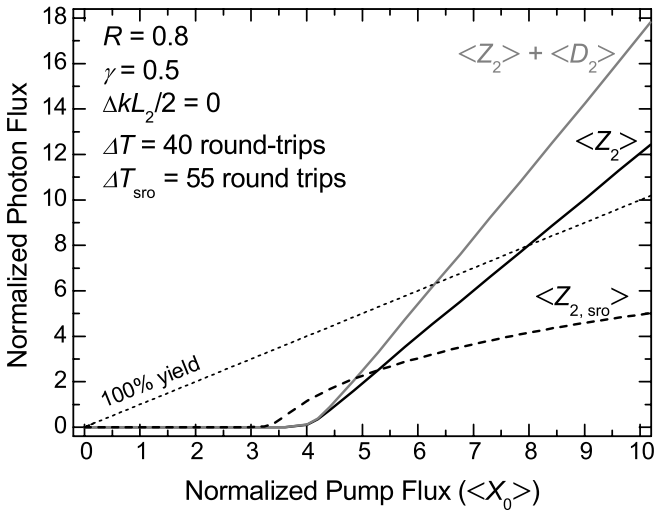

FIGURE 4 Output idler $\langle Z_2\rangle$ and idler plus difference-frequency $\langle Z_2\rangle + \langle D_2\rangle$ versus input pump $\langle X_0\rangle$ in pulsed regime for a SRO and an OPO–OPA with $\gamma = \kappa_2 L_2/(\kappa_1 L_1) = 0.5$ and perfect phase-matching in the OPA crystal

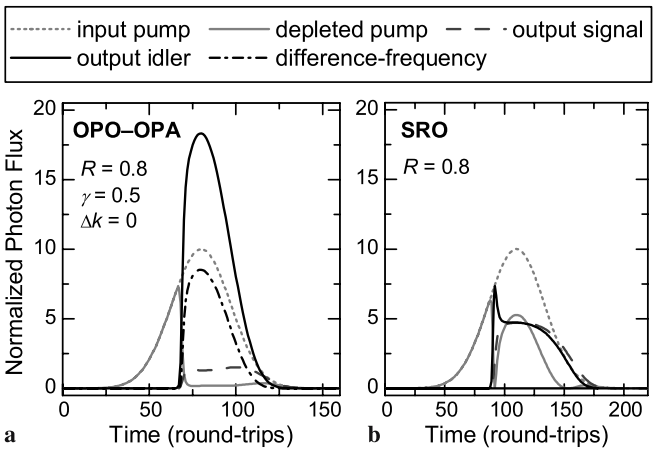

FIGURE 5 Temporal profiles of input pump, depleted pump, output signal, output idler, and difference frequency for Gaussian input pump pulses. (**a**) OPO–OPA with $\gamma = \kappa_2 L_2/(\kappa_1 L_1) = 0.5$, perfect phase-matching in the OPA crystal and $N = 40$ cavity round-trips (FWHM) and (**b**) SRO with $N_{\text{sro}} = 55$ cavity round-trips (FWHM)

2.3 *Transverse profile of the beams*

Plane wave models are helpful for understanding the physical mechanisms at stake in a pulsed OPO, such as parametric conversion and pump depletion effects. However, its is well known that this simple approach fails to give a quantitative description [17, 18]. In particular, plane-wave approaches, as the one presented above, over-estimate the saturation of the input–output characteristics of OPOs.

In order to be compared to experiments, simulation models have to take into account the spatial profile of the different beams. A very simple approach is to divide up the pump beam into a collection of independent beamlets, each of which having a nearly uniform intensity distribution over its cross section [17, 18]. Each pump beamlet is then injected into the semi-analytical model described in Sect. 2.2 to give rise to a resonant signal beamlet and to a non-resonant idler beamlet. At the end of the integration all the beamlets are summed up to get the whole beams. It should be noted, however, that this assumption holds true only if the effects of diffraction can be neglected. This is obviously the case in our plane-plane OPO cavities where all beams are collimated with a Rayleigh range much larger than the cavity length.

One should also note that, despite the rough single longitudinal-mode approximation we made, good agreement with the experience is expected because the group velocity of the three interacting waves are close to each other [19].

2.4 *Simulation results*

Using our semi-analytical model taking into account the Gaussian shape of the beams, we simulate the behavior of the three main OPO cavities studied in this work (see Sect. 3). The parameters for the simulation are taken from experimental data and measurements. No adjustment is made. For each OPO, the cavity optical length is estimated from the real cavity length and the crystals indices at the pump wavelength. The quantum noise necessary for the parametric process to start is taken to be half a photon per mode. The cavity overall reflectivity R for the resonant wave is deduced from the transmission of the different optics at the signal wavelength.

For the OPO–OPA, it is necessary to include the 1.5° walk-off angle between the signal and the idler waves in the second KTA crystal. According to [20], this walk-off can be expressed in terms of an effective interaction length between the signal and pump waves which depends on the spot sizes at these wavelengths. For a plane mirrors cavity, the steady-state spot size of the resonant wave is determined by the balance between the transverse gain profile in the crystal and diffraction of the whole beam. Still following [20], we calculate a signal waist of 315 μm in the short OPO cavity for a pump waist of 720 μm. This leads to an effective interaction length 30% smaller than the crystal physical length, and thus we reduce the γ_0 parameter by the same amount.

In the experiments, the two KTA crystals have a strong unwanted absorption of about 16% at the idler wavelength. Also, the mirrors have a small but significant reflectivity at the same wavelength. Because the idler wave is non-resonant, these losses are simply given by the overall transmission of the different optics on its path. In a more rigorous approach, the losses occurring between the OPO and the OPA processes are included by doing the following replacement in the functions developed in Sect. 2: $Z_1 \rightarrow \eta Z_1$, where η is the transmission factor.

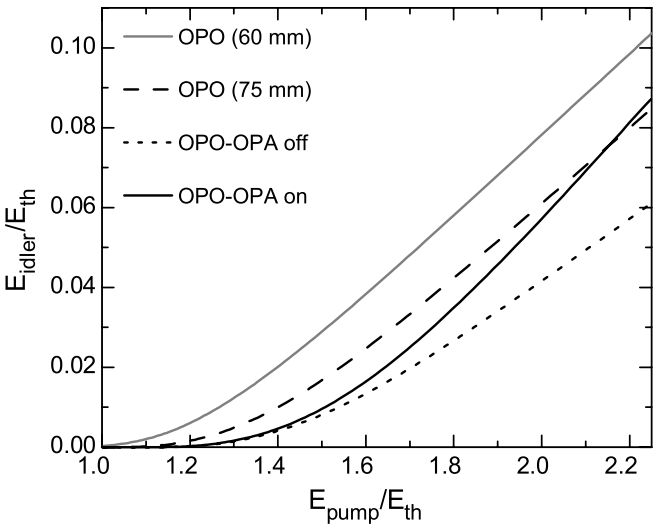

FIGURE 6 Simulated curves showing the output idler energy versus incident pump energy for the four OPO cavities studied here: the short-cavity OPO (60 mm), the long-cavity OPO (75 mm), and the OPO–OPA with (on) and without (off) phase-matching for the OPA process. The simulation is done according to Sect. 2, with parameters corresponding to the experiments related in Sect. 3

Finally, the pump temporal profile is taken to be a Gaussian with a total width at half maximum of 27.5 ns. It is nearly identical to the actual profile of the Nd:YAG laser used in the experiments.

Actually, for any of the studied OPOs the oscillation thresholds predicted by this model is far below the experimental one. This discrepancy is common with unseeded plane-plane cavities, for which both this model and more complete numerical programs fail to predict quantitatively the experimental data [21]. This systematic discrepancy has not, to our knowledge, been explained in the literature. Our simulation results are thus normalized to the computed oscillation threshold in order to be compared with the experimental results.

Our simulation results are reported in Fig. 6. As we will see later, they fairly reproduce the different behaviors of the OPO cavities studied experimentally. We will discuss this further in Sect. 4.

3 Experimental results

In order to carry out a critical study of the OPO–OPA we study several intermediate configurations from the singly-resonant OPO to the OPO–OPA architecture.

3.1 *Short-cavity* OPO

The first studied configuration is a singly resonant OPO, depicted in Fig. 7a. The 60-mm-long cavity is formed by a 20-mm-long KTA crystal and two flat mirrors M_1 and M_2. The KTA crystal is used in a Type-II, non-critical phase-matching configuration along the x-axis ($\varphi = 90°$ and $\theta = 0°$), to have both maximum effective non-linear coefficient, $d_{\text{eff}} = 3.18\,\text{pm/V}$ [22], and no walk-off between the

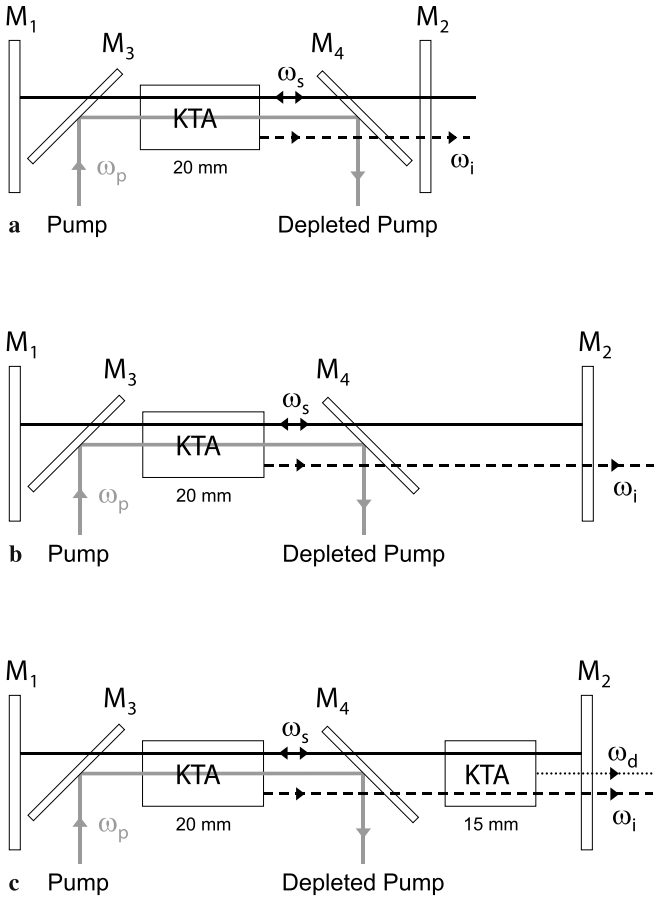

FIGURE 7 Schematic diagram of the three different OPO cavities studied in this paper: (**a**) OPO with a 60-mm-long cavity, (**b**) OPO with a 75-mm-long cavity, (**c**) OPO–OPA with a 75-mm-long cavity

pump, signal, and idler beams. Both faces of the 20-mm-long KTA crystal are antireflection coated at the signal and idler wavelengths. The cavity mirrors M_1 and M_2 are highly transmissive for the idler and highly reflective for the signal. To avoid damage of mirrors M_1 and M_2 and to prevent backward pump reflection, the pump beam enters inside the cavity by the 45° mirror M_3 and exits after the crystal by the 45° mirror M_4. These 45° mirrors are highly transmissive for the signal and the idler, and highly reflective for the pump. The spectral characteristics of the different optical components have been measured at the signal and idler wavelengths and gathered in Table 2. This measurement reveals that this KTA crystal has a strong absorption at the idler wavelength of about 17%. Since this value cannot be explained by the natural absorption in KTA, it is likely to be a problem with the coatings. The pump source is a flash-lamp pumped Nd:YAG laser ($\lambda_p = 1.064\,\mu m$), emitting 27.5 ns pulses with a 12.5 Hz repetition rate. The incident pump beam is collimated with a waist of $\sim 720\,\mu m$. The output energy is limited to ~ 90 mJ per pulse to stay below the damage thresholds of the cavity mirrors and crystal coatings.

Figure 8 shows the output idler energy as a function of the incident pump energy for the different OPO configurations studied in this work. The short-cavity OPO displays an oscillation threshold of 40 mJ and an efficiency of 7.2% at a pump energy of 86.4 mJ.

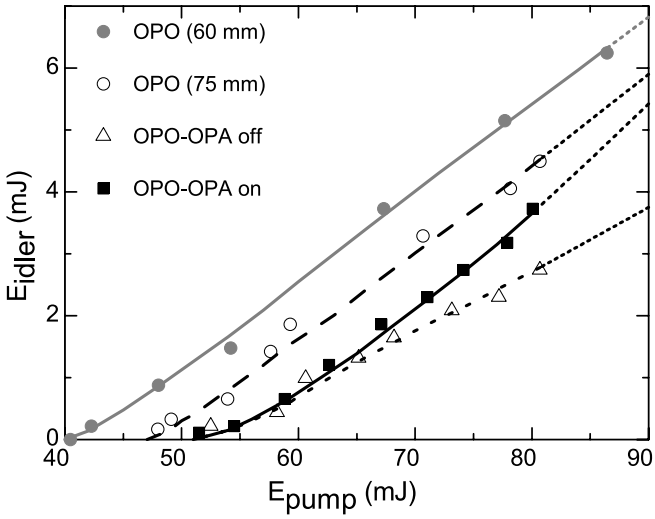

FIGURE 8 Experimental curves showing the output idler energy versus incident pump energy for the four OPO cavities of this study. *Lines* are guides for the eyes

Optics	Reflectivity (%)			Idler loss (%)
	1.54 μm	3.45 μm	2.78 μm	
M1, M2	98.5	6	48	
M3, M4	2.5	4		
KTA 20 mm	< 0.6	< 0.7		17
KTA 15 mm	< 0.2	< 0.7	83	16

TABLE 2 Spectral characteristics of the coatings

3.2 *Long-cavity* OPO

In a second step, we increase the OPO cavity length up to 75 mm as shown in Fig. 7b. This OPO displays the same slope efficiency as the short-cavity OPO but has a higher threshold of 48 mJ. Indeed, during the same amount of time, the generated idler and signal waves do less round trips in the long cavity than in the short one. Hence they experience less amplification and need more time to build up from the noise. Because of the limited duration of the pump pulses, this buildup time is detrimental to the OPO efficiency, and increases its threshold.

3.3 OPO–OPA

The OPO–OPA design is obtained by inserting a second nonlinear crystal in the cavity, as displayed in Fig. 7c. This 15-mm-long KTA crystal is used in Type-II phase-matching with $\varphi = 70°$ and $\theta = 0°$ in order to perform the OPA process $1.54–2.78\,\mu m \rightarrow 3.45\,\mu m$. The length of this second crystal is chosen to be close to the optimum value for the OPA process, as explained in Sect. 2.1. It is mounted on a rotation stage for phase-matching optimization. The OPA crystal is antireflection coated at the signal and idler wavelengths, but the coatings also displays a total absorption loss of 16% for the idler.

The OPO–OPA exhibits a threshold of 50 mJ whether the OPA process is phase-matched (OPA on) or not (OPA off). The rise of the threshold is linked to the second crystal that increases the optical length of the cavity. However, the frequency conversion in the second crystal does not affect the

OPO threshold, because it is not effective until the signal builds up in the cavity. When the OPA is off, the OPO produces 2.7 mJ of idler energy for a pump of 81 mJ, associated to 3.3% of energy efficiency. When the OPA is on, the OPO generates 3.8 mJ and 4.7% efficiency for the same pump power. Thus we obtain a 35% increase of the idler energy at the maximum available pump energy when the OPA process is phase-matched. It is important to note, however, that the OPO–OPA performance is strongly lowered by the unwanted absorption of the second KTA crystal.

The origin of this rather low efficiency is now analyzed with the support of analytical expressions and numerical simulations.

4 Discussion

The general trends deduced from the plane-wave analysis are confirmed by our experimental and simulation results, shown in Figs. 8 and 6 respectively. All of them reveal that the OPO–OPA does not output more idler energy than a single-crystal OPO for moderate pump energies (i.e., less than ~ 2 times above threshold) despite the 40% energy increase brought by the OPA process. This result clearly evidences the importance of cavity lengthening for this kind of mid-energy pulsed OPOs.

Nevertheless, for applications where it is required to use the maximum mid-infrared energy available (e.g., composite materials analysis), a very interesting feature of the OPO–OPA is that it produces an additional wavelength, according to the difference frequency process 1.54–3.45 μm → 2.78 μm. This extra radiation also leads to an enhancement of the mid-IR output and can make the OPO–OPA an interesting device even if it produces less idler output than the short-cavity OPO. We thus measure the total mid-IR output of the short-cavity OPO and the OPO–OPA. However, in our experiment the crystal and mirrors coatings transmissions at the idler and DFG wavelengths differ greatly. It is necessary to subtract these losses in order to make a fair comparison between the OPO and the OPO–OPA, which has been done in Fig. 9. Despite its higher threshold, we see that the OPO–OPA produces actually more mid-IR radiation than the short-cavity OPO for pump energies beyond 80 mJ (2× threshold).

Furthermore, we would like to emphasize that in our experiments the γ parameter is not optimum, partly because the effective length of the OPO crystal is reduced by the walk-off. Moreover, the OPO–OPA output is greatly reduced by the strong idler absorption of the OPA crystal coatings. In order to investigate the capabilities of the OPO–OPA scheme, we simulate the performances of an optimum design for the OPO–OPA configuration without detrimental absorption and with an optimized OPA crystal length of 22 mm. Simulation results for this design are reported in Fig. 10. They show that the OPO–OPA would produce more idler energy than the short-cavity OPO beyond 1.6× threshold. Also the slope efficiency is twice the one of the short-cavity OPO. However, compared to the OPO the improvement is only of 1.5 at 2.5× threshold. Again, we are mostly interested by the total energy near 3 μm, so we also have to consider the DFG output. In this case the OPO–OPA overcomes the OPO as soon as 1.4× threshold, with a slope efficiency greater by a factor of 3. When

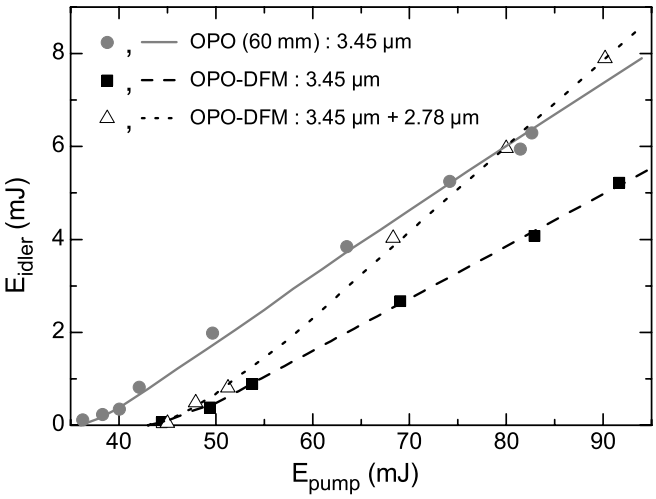

FIGURE 9 Idler energy for the short-cavity OPO (60 mm) and energy at the idler (3.45 μm) and DFG (2.78 μm) wavelengths for the OPO–OPA versus incident pump energy. The *dots* are experimental data while the *curves* are guides for the eyes. Losses due to the second face of the OPA crystal and to the end cavity mirror M_2 have been subtracted

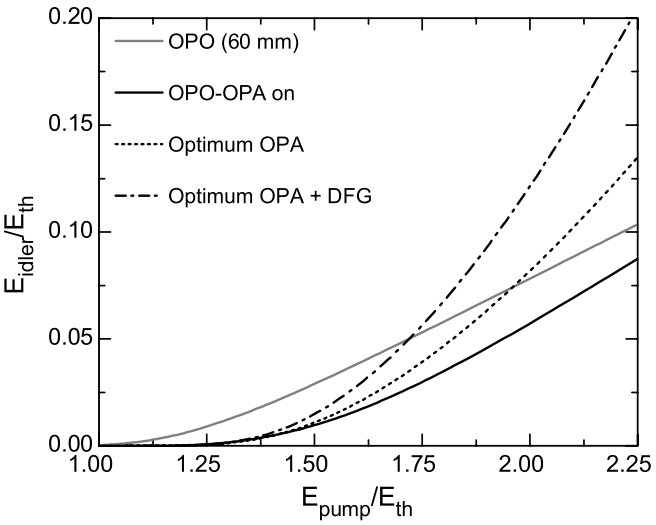

FIGURE 10 Simulated curves showing the output idler energy versus incident pump energy for the short-cavity OPO (60 mm), the OPO–OPA as studied experimentally, and the OPO–OPA with an optimum design. The total output mid-IR energy (idler + DFG) is also shown for the optimum OPO–OPA

pumped 2 times above threshold, the OPO–OPA would produce twice more energy around 3 μm than the short-cavity OPO. We should point out that the idler and DFG wavelengths can be made the same by changing the phase matching angles in the two crystals. In this case, the signal would be at 1.6 μm and the idler at 3.19 μm.

5 Conclusion

In this paper, we investigated both experimentally and theoretically the pros and cons of the OPO–OPA versus the OPO in pulsed regime.

If the output is restricted to the idler, an optimum OPO–OPA has to be pumped 2× beyond threshold to become beneficial. Higher pumping levels ($\sim 3\times$ threshold) are necessary for the gain to become substantial. The conclusion is quite

different if the total output near 3 μm is available for the application. Experimental results obtained with a non optimum design show that the OPO–OPA outputs more 3 μm energy than the OPO when pumped 2× beyond threshold. Our simulations of an optimum design of the OPO–OPA show that it would produce twice more energy at the same pumping level. In order to achieve this, the relative lengths of the two crystals have to be chosen carefully and should take into account the walk-off and/or the phase mismatch in the crystals. In this case, the OPO–OPA is an efficient device that may be very convenient for many applications, such as laser ultrasound generation that requires high energy pulses in the mid-infrared.

Appendices

A Expressions of the parametric gain in the two crystals

In this appendix, we give the analytical expressions of the gain experienced by the signal (idler) wave in the first (second) crystal.

As explained in Sect. 2.1, one can derive exact solutions of the coupled nonlinear equations describing the propagation of the three waves in the crystals following the approach introduced in [10]. With the same notations as in [11], the parametric gain $G_1(X_0, Y_0) = Y_1/Y_0$ experienced by signal Y from z_0 to z_1 is given by

$$G_1(X_0, Y_0) = 1 - \mathrm{sn}^2\left(\mathrm{i}\,\mathrm{arccosh}\left(\frac{1}{\sqrt{R}}\right)\sqrt{X_0}\,\middle|-\frac{Y_0}{X_0}\right), \tag{A.1}$$

where the Jacobi inverse function sn is defined by [23]

$$a\int_0^x \frac{\mathrm{d}t}{\left[\left(a^2-t^2\right)\left(b^2-t^2\right)\right]^{1/2}} = \mathrm{sn}^{-1}\left(\frac{x}{b}\,\middle|\,\frac{b^2}{a^2}\right). \tag{A.2}$$

In the same way, one can find after some algebra the parametric gain $G_2(Y_1, Z_1, \Theta) = Z_2/Z_1$ experienced by the idler wave from z_1 to z_2:

$$G_2(Y_1, Z_1, \gamma, \Theta) = 1 - \frac{\tilde{Z}_1}{Z_1} \times \mathrm{sn}^2\left(\mathrm{i}\gamma\,\mathrm{arccosh}\left(\frac{1}{\sqrt{R}}\right)\sqrt{\tilde{Y}_1}\,\middle|-\frac{\tilde{Z}_1}{\tilde{Y}_1}\right), \tag{A.3}$$

where $\gamma = \kappa_2 L_2/\kappa_1 L_1$ is the ratio of the nonlinear drives of the second crystal (OPA) to the first crystal (OPO). $\tilde{Y}_1$ and $\tilde{Z}_1$ are given by

$$\tilde{Y}_1 = \frac{1}{2}\left\{Y_1 - Z_1 - \Theta^2 + \left[\left(Y_1+Z_1\right)^2 - 2\Theta^2\left(Y_1 - Z_1 - \frac{\Theta^2}{2}\right)\right]^{1/2}\right\}, \tag{A.4}$$

and

$$\tilde{Z}_1 = \frac{1}{2}\left\{Z_1 - Y_1 + \Theta^2 + \left[\left(Y_1+Z_1\right)^2 - 2\Theta^2\left(Y_1 - Z_1 - \frac{\Theta^2}{2}\right)\right]^{1/2}\right\}, \tag{A.5}$$

where the effect of imperfect phase-matching in the OPA crystal is included through the dimensionless phase-mismatch parameter Θ given by

$$\Theta = \frac{\Delta k L_2/2}{\gamma\,\mathrm{arccosh}\left(1/\sqrt{R}\right)}. \tag{A.6}$$

In the case of perfect phase-matching ($\Theta = 0$), $\tilde{Y}_1$ and $\tilde{Z}_1$ reduce to Y_1 and Z_1 respectively.

B Expression of normalized output flux

In this appendix, we give the expression of depleted pump X_2, output signal $(1-R)\,Y_2$, output idler Z_2, and output difference-frequency D_2 as functions of X_0 and Y_0:

$$X_2 = X_0 - Y_0\left[G_1(X_0, Y_0) - 1\right], \tag{B.1}$$

$$Y_2 = Y_0 G(X_0, Y_0, \Theta), \tag{B.2}$$

$$Z_2 = Y_0\left[G_1(X_0, Y_0) - 1\right] \times G_2\left\{G_1(X_0, Y_0)\,Y_0, \left[G_1(X_0, Y_0) - 1\right]Y_0, \Theta\right\} \tag{B.3}$$

and

$$D_2 = Y_0\left[G_1(X_0, Y_0) - G(X_0, Y_0, \Theta)\right]. \tag{B.4}$$

C Optimal ratio of the nonlinear couplings

As explained in Sect. 2.1, quasi complete pump depletion (CPD) can be achieved over a large dynamic range with the OPO–OPA if the proper conditions are fulfilled.

To achieve CPD for a given value of the input pump flux X_0, the value of the signal flux $Y_0 = Y_0^{\mathrm{cpd}}$ at the OPO crystal entrance must lead to $X_1 = 0$, i.e.,

$$Y_0^{\mathrm{cpd}}\left[G_1\left(X_0, Y_0^{\mathrm{cpd}}\right) - 1\right] = X_0, \tag{C.1}$$

where (B.1) was used. For high mirror reflectivities, i.e., when $\delta = 1 - R \to 0$, an asymptotical expression may be derived from (C.1). With the approximation $\mathrm{arcosh}\left(1/\sqrt{1-\delta}\right) \approx \sqrt{\delta}$ and using the cw output signal $Y' = (1-R)\,Y_0^{\mathrm{cpd}}/R$ in the equations, the CPD condition (C.1) may the be rewritten

$$-\mathrm{sn}^2\left[\mathrm{i}\sqrt{\delta X_0}\,\middle|-\frac{Y'}{\delta X_0}\right] = \frac{\delta X_0}{Y'}, \tag{C.2}$$

The asymptotical value of this latter expression can be obtained using the following transformation [23]

$$\mathrm{sn}(u\,|-m) = \sqrt{\mu_1}\,\mathrm{sd}(v\,|\mu), \tag{C.3}$$

where $\mu = m/(1+m)$, $\mu_1 = 1/(1+m)$, and $v = u/\sqrt{\mu_1}$. Using also the relation $\mathrm{sd}(u\,|1) = \sinh(u)$, (C.2) simplifies dramatically

$$\sin^2\left(\sqrt{Y'}\right) = 1. \tag{C.4}$$

CPD is thus achieved for $Y' = \pi^2/4$.

The second step of the calculation is to derive the expression of the optimal nonlinear couplings ratio $\gamma_{\rm cpd}$ that yields to $Y_0 = Y_0^{\rm cpd}$ at the OPO crystal entrance when the OPO–OPA is oscillating. Assuming that condition (C.1) is satisfied, oscillation condition (5) may be written

$$G_2\left(X_0 + \frac{R}{(1-R)}Y', X_0, \gamma_{\rm cpd}, \Theta\right) = 2 - \frac{Y'}{X_0}\,. \tag{C.5}$$

When $\delta = 1 - R \to 0$, one can perform a first order expansion on δ to simplifies expression (A.3) of function G_2. Two cases have then to be considered,

– first case: $Y' \geq \Delta k L_2/2$, the first order expansion gives

$$G_2\left(X_0 + \frac{Y'}{\delta}, X_0, \gamma_{\rm cpd}, \frac{\Delta k L_2}{2\sqrt{\delta}}\right) \to 1 + \frac{4\gamma_{\rm cpd}^2 Y'}{4\gamma_{\rm cpd}^2 Y' - (\Delta k L_2)^2} \sinh^2\left(\sqrt{\gamma_{\rm cpd}^2 Y' - \frac{(\Delta k L_2)^2}{4}}\right); \tag{C.6}$$

– second case: $Y' < \Delta k L_2/2$, using transformation (C.3), one obtains

$$G_2\left(X_0 + \frac{Y'}{\delta}, X_0, \gamma_{\rm cpd}, \frac{\Delta k L_2}{2\sqrt{\delta}}\right) \to 1 + \frac{4\gamma_{\rm cpd}^2 Y'}{(\Delta k L_2)^2 - 4\gamma_{\rm cpd}^2 Y'} \sin^2\left(\sqrt{\frac{(\Delta k L_2)^2}{4} - \gamma_{\rm cpd}^2 Y'}\right). \tag{C.7}$$

Using (C.5) and the well-known relation $\sinh(u) = -\mathrm{i}\sin(\mathrm{i}u)$, the two above cases lead to the same implicit relation for $\gamma_{\rm cpd}$:

$$\gamma_{\rm cpd} = \frac{2}{\pi}\left[1 - \left(\frac{\Delta k L_2}{\pi\gamma_{\rm cpd}}\right)^2\right]^{-1/2} \times \operatorname{arcsinh}\left\{\left(1 - \frac{\pi^2}{4X_0}\right)^{1/2}\left[1 - \left(\frac{\Delta k L_2}{\pi\gamma_{\rm cpd}}\right)^2\right]^{1/2}\right\}. \tag{C.8}$$

D Optimal ratio of the nonlinear couplings in the mean-field approximation

For high mirror reflectivities, the intracavity power of the signal wave is very high compared to the idler and pump waves. Thus we can consider it as a constant when integrating the nonlinear coupling equations for the pump and idler waves: $Y(z) \simeq Y_0$. In this so-called mean-field approximation, the expression for the depleted pump X_1 after the first crystal is

$$X_1 = X_0 \cos^2\left[\operatorname{arccosh}\left(\frac{1}{\sqrt{R}}\right)\sqrt{Y_0}\right]. \tag{D.1}$$

The signal flux for complete pump depletion after the first crystal, $X_1 = 0$, is thus given by

$$Y_0 = \frac{(\pi/2)^2}{\operatorname{arccosh}^2\left(\frac{1}{\sqrt{R}}\right)}\,. \tag{D.2}$$

The quantity $X + Y$ is a constant of motion, that is $X_1 + Y_1 = X_0 + Y_0$. Hence the signal flux after the first crystal is

$$Y_1 = Y_0 + X_0 \sin^2\left[\operatorname{arccosh}\left(\frac{1}{\sqrt{R}}\right)\sqrt{Y_0}\right]. \tag{D.3}$$

In the mean-field approximation, the power of the difference frequency wave after the second crystal is given by

$$D_2 = X_0 \sin^2\left[\operatorname{arccosh}\left(\frac{1}{\sqrt{R}}\right)\sqrt{Y_0}\right] \times \sinh^2\left[\gamma\operatorname{arccosh}\left(\frac{1}{\sqrt{R}}\right)\sqrt{Y_0}\right] \tag{D.4}$$

where, for simplicity's sake, we assume perfect phase-matching in the second crystal. Consequently, the remaining signal power is

$$Y_2 = Y_0 + X_0 \sin^2\left[\operatorname{arccosh}\left(\frac{1}{\sqrt{R}}\right)\sqrt{Y_0}\right] \times \left\{1 - \sinh^2\left[\gamma\operatorname{arccosh}\left(\frac{1}{\sqrt{R}}\right)\sqrt{Y_0}\right]\right\}. \tag{D.5}$$

The oscillation condition in the steady-state regime is $RY_2 = Y_0$. Combining (D.2) and (D.5) leads to

$$\gamma_{\rm cpd} = \frac{2}{\pi}\operatorname{arcsinh}\left[\left(1 - \frac{\pi^2}{4X_0}\right)^{1/2}\right]. \tag{D.6}$$

This expression is identical to (C.8) for perfect phase-matching. Using the relation $\cosh(2x) = 1 + 2\sinh^2(x)$, one can reduce the above equation to

$$\gamma_{\rm cpd} = \frac{1}{\pi}\operatorname{arccosh}\left(3 - \frac{\pi^2}{2X_0}\right). \tag{D.7}$$

One should note that the above mean-field calculation can be straightforwardly generalized ro imperfect phase-matching in the second crystal, leading to the same expression as (C.8).

ACKNOWLEDGEMENTS This work has been carried out under European contract INCA (project GRD1-2000-25309)

REFERENCES

1 K.L. Vodopyanov, *Solid-State Mid-Infrared Sources*, ed. by I.T. Sorokina, K.L. Vodopyanov (Springer, Berlin Heidelberg, 2003), pp. 141–178
2 C.B. Scruby, L.E. Drain, *Laser Ultrasonics: Techniques and Applications* (Hilger, Bristol, 1990)
3 D.A. Hutchins, *Review of Progress in QNDE*, ed. by D.O. Thomson, D.E. Chimenti, vol. 11 (Plenum, New York, 1992), p. 561
4 J.P. Monchalin, *Review of Progress in QNDE*, ed. by D.O. Thompson, D.E. Chimenti, vol. 12A (Plenum, New York, 1993), p. 465
5 M. Dubois, P.W. Lorraine, R.J. Filkins, T.E. Drake, Appl. Phys. Lett. **79**, 1813 (2001)
6 K. Koch, G.T. Moore, E.C. Cheung, J. Opt. Soc. Am. B **12**, 2268 (1995)

7 M.E. Dearborn, K. Koch, G.T. Moore, Opt. Lett. **23**, 759 (1998)
8 J.M. Fukumoto, H. Komine, W.H. Long Jr., E.A. Stappaerts, *Advanced Solid-State Lasers*, ed. by W.R. Bosenberg, M.M. Fejer, vol. 19 of OSA Trends in Optics and Photonics (Optical Society of America, Washington, DC, 1998), p. 245
9 I. Lee, W.J. Alford, J. Bartholomew, *Advanced Solid-State Photonics*, ed. by C. Denman, I. Sorokina, vol. 98 of OSA Trends in Optics and Photonics (Optical Society of America, Washington, DC, 2005), p. 444
10 J.A. Armstrong, N. Bloembergen, J. Ducuing, P.S. Pershan, Phys. Rev. **127**, 1918 (1962)
11 E. Rosencher, C. Fabre, J. Opt. Soc. Am. B **19**, 1107 (2002)
12 A. Godard, E. Rosencher, IEEE J. Quantum Electron. **QE-40**, 1527 (2004)
13 P.P. Bey, C.L. Tang, IEEE J. Quantum Electron. **QE-8**, 361 (1972)
14 K.D. Shaw, Opt. Commun. **144**, 134 (1997)
15 E. Granot, S. Pearl, M.M. Tilleman, J. Opt. Soc. Am. B **17**, 381 (2000)
16 A. Godard, M. Raybaut, O. Lambert, J.-P. Faleni, M. Lefebvre, E. Rosencher, J. Opt. Soc. Am. B **22**, 1966 (2005)
17 J.E. Bjorkholm, IEEE J. Quantum Electron. **QE-7**, 109 (1971)
18 T. Debuisschert, Quantum Semiclass. Opt. **9**, 209 (1997)
19 G. Arisholm, G. Rustad, K. Stenersen, J. Opt. Soc. Am. B **18**, 1882 (2001)
20 S.J. Brosnan, R.L. Byer, IEEE J. Quantum Electron. **QE-15**, 415 (1979)
21 A.V. Smith, W.J. Alford, T.D. Raymond, M.S. Bowers, J. Opt. Soc. Am. B **12**, 2253 (1995)
22 D.N. Nikogosyan, *Nonlinear Optical Crystals: A Complete Survey* (Springer, New York, 2005)
23 M. Abramowitz, I. Stegun, *Handbook of Mathematical Functions* (Dover, New York, 1970)